RSC Advances

PAPER

View Article Online
View Journal | View Issue

Cite this: RSC Adv., 2016, 6, 42502

Dielectric investigation of the Sr_3WO_6 double perovskite at RF/microwave frequencies

D. V. M. Paiva,[a] M. A. S. Silva,[b] A. S. B. Sombra[b] and P. B. A. Fechine*[a]

Received 21st February 2016
Accepted 21st April 2016

DOI: 10.1039/c6ra04640a

www.rsc.org/advances

This work reports the dielectric properties of Sr_3WO_6 (SWO) double perovskite at radio frequencies as a function of the temperature and a study in microwaves range to evaluate the material as a novel dielectric resonator. Thermo-activated charge transfer process for SWO ceramic was observed and two resistor–capacitor associations were fitted for the Nyquist diagram. SWO presented negative values of temperature coefficient of capacitance (TCC) and the activation energies of dielectric relaxation processes were measured by conductivity (1.35 eV), imaginary modulus (1.38 eV) and imaginary impedance (1.36 eV). For the microwave range, SWO shows high dielectric permittivity (13.57) and dielectric loss (0.0281). The dielectric resonator antenna (DRA) fabricated from SWO ceramic presented an operation frequency in 4.1 GHz and return loss below −40 dB. It was possible to evaluate the performance of the antenna from numerical simulation. From these results, the SWO based DRA shows good properties to be used as a novel microwave dielectric resonator.

1. Introduction

Ceramic oxides with structural formula $A_2B'B''O_6$ are called double perovskite. In this kind of structure, the A site generally is a large divalent cation twelve-coordinated and B′ and B″ sites are octahedral-coordinated with varied oxidation state and commonly occupied by transition metal ions. The double perovskite presents a large number of different compositions, as a wide combination of ions in the B′ and B″ sites, where the final combination must be a sum of charges equal to 8+ or the necessary charge for complete electroneutrality of the structure due to the charges of A site (Ca^{2+}, Sr^{2+}, Li^{+}, La^{3+} *etc.*).[1] In this sense, different applications can be obtained by changing in these sites. For example, La_2NiMnO_6 nanoparticles[2] have been studied for a potential carrier for large biomolecules, $Sr_2B'MoO_6$ (B′ = Mg, Mn, Fe, Co, Ni and Zn)[3–5] has been found to be a promising compound as an anode material for solid-oxide fuel-cell (SOFCs) and Bi_2NiMnO_6 presents multiferroic properties at low temperature with potential as nonvolatile memories and sensors.[6] Pang and Zhou[7] investigated Ca_3WO_6 phase, which presented good results for potential microwave applications,[8,9] becoming important for development in wireless communication systems, miniaturization of components such as dielectric filters, and voltage-controlled oscillators.

Sr_3WO_6 (SWO) is another example of double perovskite that has two Sr^{2+} ions in site A and one Sr^{2+} and W^{6+} ions distributed in the B′ and B″ sites. SWO presents four polymorphs (α, β, γ and δ) from low to high temperature.[10] This material has been traditionally studied due to luminescence properties: the photoluminescence and thermoluminescence properties of Sr_3WO_6:Eu^{3+} was reported by Emen and Altinkaya,[11] while Zhigang Zou *et al.*[12] obtained an efficient charge compensated red phosphor for Sr_3WO_6:K^{+},Eu^{3+} for white LEDs. However, the SWO perovskite structure are also an important oxide class for dielectric materials with calcium, strontium and barium titanate, the most representative of perovskite structure for dielectric properties.

In this work, the best set of parameters to synthesize the SWO phase by solid-state route was achieved by X-ray diffraction (XRD). The dielectric properties of the material were measured at radio frequency as a function of the temperature (298–718 K). For microwave applications, SWO was experimentally measured as a dielectric resonator and supported by numerical simulation. The results set can be used to suggest potential novel applications for SWO phase as a dielectric resonator antennas (DRA) or other devices that operate in the microwaves range (microwave filters, oscillators, radar detectors *etc.*).

2. Experimental methods

The synthesis of the SWO phase was performed by a solid state route, where stoichiometric amounts of the precursors employed in the process were $SrCO_3$ (97%, Vetec) and WO_3 (99%, Aldrich). These starting materials were activated by milling in the planetary mill, on a Fritsch pulverisette 6, for 2 h with zirconia balls and polyacetal jars. The activated powder

[a]Grupo de Química de Materiais Avançados (GQMAT), Departamento de Química Analítica e Físico-Química, Universidade Federal do Ceará – UFC, Campus do Pici, CP 12100, CEP 60451-970 Fortaleza, CE, Brazil. E-mail: fechine@ufc.br

[b]Laboratório de Telecomunicações e Ciência e Engenharia de Materiais (LOCEM), Departamento de Física, Universidade Federal do Ceará, Brazil

was calcined in air at 1323, 1423 and 1523 K for 6 h. The reactions occurring during calcination can be summarized as:

$$3SrCO_3 + WO_3 \rightarrow Sr_3WO_6 + 3CO_2$$

$$3SrCO_3 + WO_3 \rightarrow (Sr_3WO_6)_{1-x} + (SrWO_4)_x + (SrO)_{2x} + 3CO_2$$

The second reaction shows a spurious phase ($SrWO_4$) and SrO (from decomposition of strontium carbonate). This probable reaction was observed for sample synthesized at 1323 K. However, SrO phase was not detected due to the small concentration and weak diffraction peak compared than Sr_3WO_6 and $SrWO_4$. Thus, it was not taken into account for crystal structure refinement (see XRD results).

The preparation of the samples for dielectric measurements consisted of the fabrication of pellets and a cylindrical ceramic. Thus, SWO powder was molded into a steel die by uniaxial press and its green body sintering at two steps (773 K for 2 h and after at 1523 K for 6 h). The pellets and cylinders were polished after the sintering process. For analysis by Impedance Spectroscopy (IS), both faces of the ceramic pellet were covered with a silver conductive electrode to form a parallel face capacitor geometry. The dimensions of the pellets in dielectric were 14.04 mm of diameter and 7.34 mm of thickness for the microwave range, and 14.30 mm of diameter and 1.56 mm of thickness for the radio frequency range.

The diffractograms were obtained by PANalytical diffractometer (Xpert Pro MPD) operating at 40 kV and 45 mA in the geometry of Bragg–Brentano, with a Cu tube ($K\alpha_1 = 1.540562$ Å, $K\alpha_2 = 1.54439$ Å) at room temperature (~300 K), from crushed samples of SWO in three different temperatures (1323, 1423 and 1523 K). The diffraction patterns were obtained from 15° to 65° (2θ) at a step size of 0.013°, with the analysis time at each step (70 s) in a graphite monochromator and in the plane geometry for diffracted beam. The Rietveld method's[13] was used for obtain the refinements through the DBWS Tools software,[14] where the refined parameters were the lattice parameters, scale factor, background, U and X parameters, and overall thermal factors. The Inorganic Crystal Structure Database (ICSD) was used to identify what phases were present in the samples.

The IS data (radiofrequency range) were collected in the Solartron 1260 Impedance Analyzer at different temperatures (298–718 K). For this propose, the electric properties of the SWO was represented in terms of the: complex dielectric constant $\varepsilon^*(\omega) = \varepsilon' - j\varepsilon''$, complex impedance $Z^*(\omega) = Z' - jZ''$, electric conductivity $\sigma^*(\omega) = 1/Z^* = \sigma' + j\sigma''$, electric modulus $M^*(\omega) = 1/\varepsilon^*(\omega) = M' + jM''$ and loss tangent tan $\delta = \varepsilon''/\varepsilon'$, where (′) and (″) represents the real and imaginary part, respectively. Where $j = \omega C_0 Z^*$ and the vacuum capacitance is represented C_0 and $j = \sqrt{-1}$.[15,16] Nyquist diagrams were obtained by fitting using the Eisanalyser software.

The Hakki–Coleman method[17,18] was used for dielectric measurements in the microwave range. For antenna applications, the ceramic cylinder was placed in a ground plane (copper sheet). The device was fed by a 50 Ω coaxial cable and SMA connector, as shown in Fig. 1.

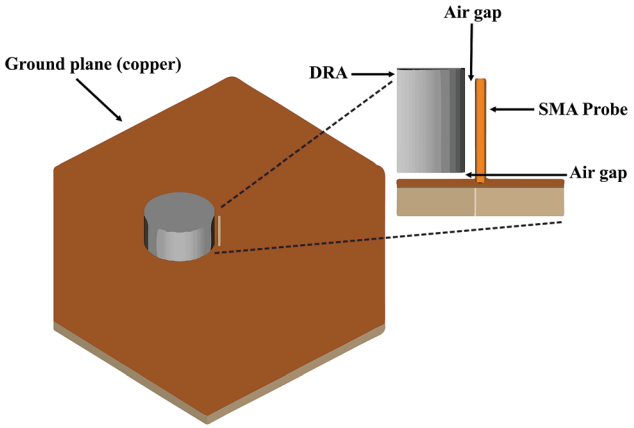

Fig. 1 Physical layout of the DRA displaying various components.

Both measurements, by Hakki–Coleman method and by antenna configuration, were undertaken with an Agilent Network Analyser, model N5230A, at room temperature. Using numerical simulations *via* the High Frequency Structure Simulator (HFSS) of Ansoft, the electromagnetic fields generated by DRA were obtained by simulation of a perfect cylinder model above a perfect ground plane. The air gaps were inserted in the model targeting for approximation of real case between numerical and experimental data from HE11δ mode. Thus, the cylindrical DRA can be approximately by the following equation:

$$f_{HE11\delta} = \frac{6.324c}{2\pi a\sqrt{\varepsilon + 2}}\left[0.27 + 0.36\left(\frac{a}{2h}\right) + 0.02\left(\frac{a}{2h}\right)^2\right] \quad (1)$$

where $f_{HE11\delta}$ (GHz) is the measured resonance frequency and c is the velocity of light in the vacuum (299 792 458 ms^{-1}), and a (m) is the radius and h (m) is the height of the cylindrical DRA (Fig. 1).

3. Results and discussion

Structural characterization was performed by the XRD technique, where it was analyzed the SWO phase formation and/or reagents and presence of spurious phase in the obtained products. The Rietveld refinement was performed for validation of the observed phases in the tested temperatures. The residuals indicators, R_{Bragg}, S (quality factor, "goodness of fit") and R_{wp} (weighted residual error), showed a satisfactory refinement and that obtained values are adequate in the range of acceptable values ($R_{wp} < 20$ and $S < 1.6$). For the R_{Bragg}, the values are closer to the acceptable limits due to the experimental conditions.[19,20] The results of the refinement are showed in the Fig. 2, where the black dots and red lines are used for represent the experimental and calculated data, respectively. The blue line is the difference between the experimental and calculated intensity. For the sample obtained at 1323 K (incomplete reaction), diffraction peaks for SWO (ICSD: 24-7338, triclinic, C1) and an intermediate phase $SrWO_4$ (ICSD: 15-5425, tetragonal, C_{4h}^6) were observed. For

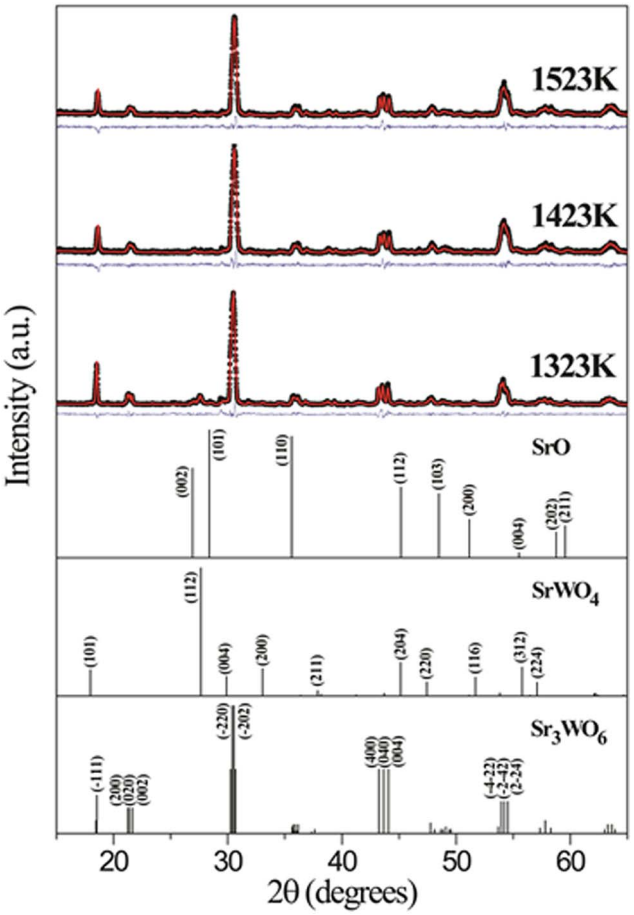

Fig. 2 XRD partner and Rietveld refinement of the SWO samples obtained in different calcination temperatures, where black dots and red line are the experimental and calculated intensity, respectively. The difference between experimental and calculated is represented by blue line.

samples synthesized at 1423 and 1523 K, the diffractograms showed peaks only for SWO. The crystalline profile of the analyzed phases are also illustrated in Fig. 2.

All refinements match with the experimental diffraction profile and there is not significant noise intense in the blue line (Fig. 2). Thus, the refinements were satisfactory, as demonstrate parameters derived from the Rietveld refinement (Table 1), where the lattice parameters, cell volume and density showed no significant changes. One can also observe a small concentration of $SrWO_4$ (6.62% wt) for the sample synthesized at 1323

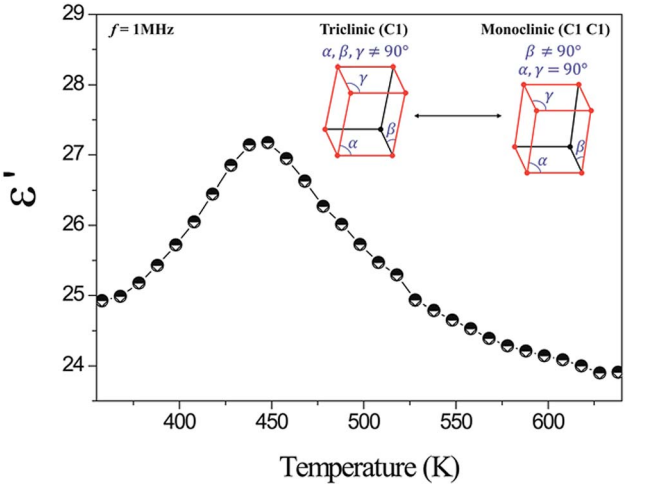

Fig. 3 Dielectric permittivity (ε') measured at 1 MHz as a function of the temperature and the representative picture of phase transition (inset).

K. Thus, the phase obtained at 1423 K was chosen for the course of the work due to lower energy involved in the process.

Complex impedance spectroscopy (CIS) technique was used for analyzing the electric response of SWO ceramic under influence of the variation of frequency as a function of the temperature, and investigate the dielectric behavior. By measurements of CIS is possible find the phase transitions of the materials. In this sense, dielectric permittivity (ε') was measured at 1 MHz and plotted as a function of the temperature (Fig. 3). It can be seen a maximum value for ε' at 445 K, corresponding to the transition temperature observed in literature,[21,22] where the SWO transits of triclinic for monoclinic symmetry, *i.e.*, the γ ↔ β phase transition. King and coworkers[10] observed the same phenomena by using electron diffraction, synchrotron X-ray powder diffraction and neutron powder diffraction.

The dielectric characterization in the radiofrequency region as a function of the temperature (298–718 K) was used to investigate the changes in the dielectric behavior of the material. Fig. 4(a) and (c) present the ε' profile and show two behavior before and after the transition temperature (445 K). Before the phase transition, ε' values presented a decrease behavior when the temperature increases, as demonstrated by values of temperature coefficient of capacitance (TCC). This behavior is probably due to the triclinic SWO, where negatives values were

Table 1 Parameters obtained from Rietveld refinement of the samples SWO synthesized at 1323, 1423 and 1523 K

Sample	Phase	Lattice parameters			R_{wp} (%)	R_{Bragg}	S	V_{cell}	Quantitative phase analysis (% wt)	Density (g cm^{-3})
		a (Å)	b (Å)	c (Å)						
SWO (1323 K)	Sr_3WO_6	10.093290	17.646570	11.813420	10.23	7.14	1.55	1714.028	93.38	6.311
	$SrWO_4$	5.414999	5.414999	12.052610		8.17		353.409	6.62	6.306
SWO (1423 K)	Sr_3WO_6	10.092880	17.642370	11.814300	12.60	9.64	1.11	1713.669	100.0	6.312
SWO (1523 K)	Sr_3WO_6	10.097800	17.649710	11.815720	12.59	8.81	1.07	1715.148	100.0	6.307

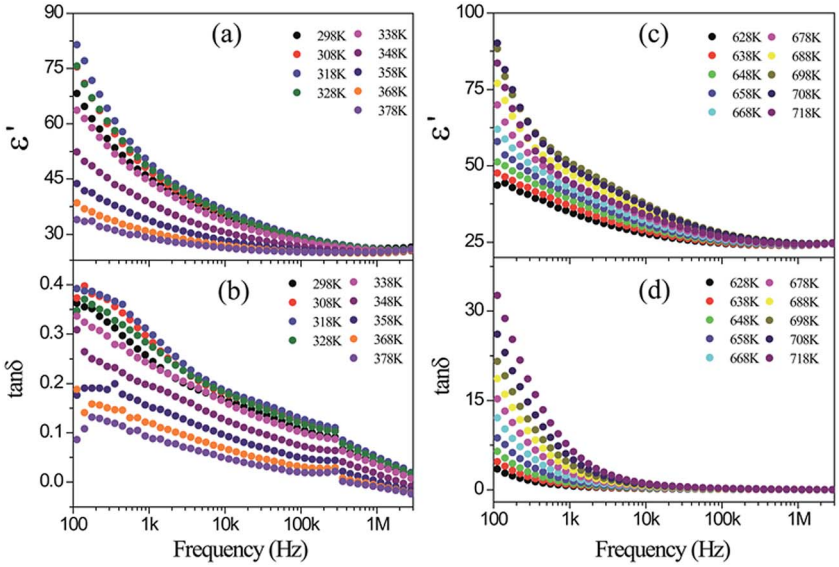

Fig. 4 Dielectric spectra at 298–718 K: (a) and (c) for constant (ε'); and (b) and (d) for dielectric loss (tan δ).

Table 2 Temperature coefficient of capacitance (TCC) of the SWO at 100, 1k, 100k and 1 MHz

Frequency (Hz)	TCC (ppm $^{\circ}C^{-1}$)
100	−6156.52
1k	−4474.66
100k	−1539.27
1 M	−471.73

obtained (Table 2). After transition temperature, the dielectric permittivity increases proportionally with the temperature. In this case, positive values of TCC can be obtained and shows the characteristics of monoclinic SWO. These values can be explained by increasing of polarization with the change of symmetry of SWO with increasing of temperature, where the highest temperature promotes a higher polarization[23] or increasing of conductivity due to the mechanism of conduction activated by temperature. The tan δ profile (Fig. 4(b) and (d)) presents similar behavior when compared to ε' values.

Some process activated by temperature are analyzed by shift of maximum frequency in the $M''(f)$, $\varepsilon''(f)$, $Z''(f)$ diagrams or by conductivity with temperature variation. Fig. 5(a)–(c) show measurements of conductivity (σ'_{ac}), imaginary modulus (M'') and imaginary impedance (Z'') as a function of the temperature (after phase transition, 608–718 K). The activation energy (E_a) for this thermo-activated process was calculated by shifting frequency of maximum frequency and the values for this thermo-active process were about 1.3 eV. Some double perovskites present smaller values than SWO, as $La_2Co_{1+x}(Mg_yTi_{1-y})_{1-x}O_6$ (E_a = 0.77–0.81 eV),[24] $BaPrCoTaO_6$ (E_a = 0.35–0.38 eV),[25] $BaLaMnSbO_6$ (E_a = 0.49–0.51 eV),[26] Sr_2CeTaO_6 (E_a = 0.78 eV),[27] $BaPrCoNbO_6$ (E_a = 0.4 eV)[28] and $Sr_2MgMoO_{6-\delta}$ (E_a = 0.52 and 1.43 eV).[29] Therefore, the thermo-active process requires more energy for SWO. The analysis of the E_a by three different methods showed values very close to each other and they are indicate of the same phenomenon.

The global dielectric and electric properties in the ceramic may be sum of contributions as electric and/or dielectric response provide by grain, grain boundary or electrode. The analysis of Nyquist diagram enables the visualization of this contribution. This model can be seen by fitting with equivalent circuit method or by models (Cole–Cole, Cole-Davidson *etc.*) or by well defined semi-circle. The impedance measurements showed the presence of semicircle, where these results were fitted by equivalent circuit model. Although of this results show only one semicircle, it was necessary to use two associated RC for best fitting. Fig. 6(a) demonstrates the experimental and obtained Nyquist diagram following this methodology. The fittings presents good correlation with experimental data. Fig. 6(b) shows the equivalent circuit for SWO, where it can be seen two resistor–capacitor (RC) circuit. They are associated with the grain (C_g and R_g) and grain boundary (C_{gb} and R_{gb}) of the ceramics. In these associations were utilized Constant Phase Element (CPE) instead of capacitance and it is well justified by increasing of conductivity of ceramic with temperature and the impedance values decreasing with temperature. Table 3 summarizes the fitting value of parameters used in equivalent circuit. The R, P and N parameters were obtained by fitting and presents different values, dependent on the temperature. For example, the resistances R_1 and R_2 decrease when the temperature increase due to the increased conductivity. However, the N parameter decreased with temperature, since the material becomes more conductive and the capacitive characteristic ceases. The parameter are marked by subscript numbers 1 and 2. They are assigned to grain and grain boundary parameters, respectively.

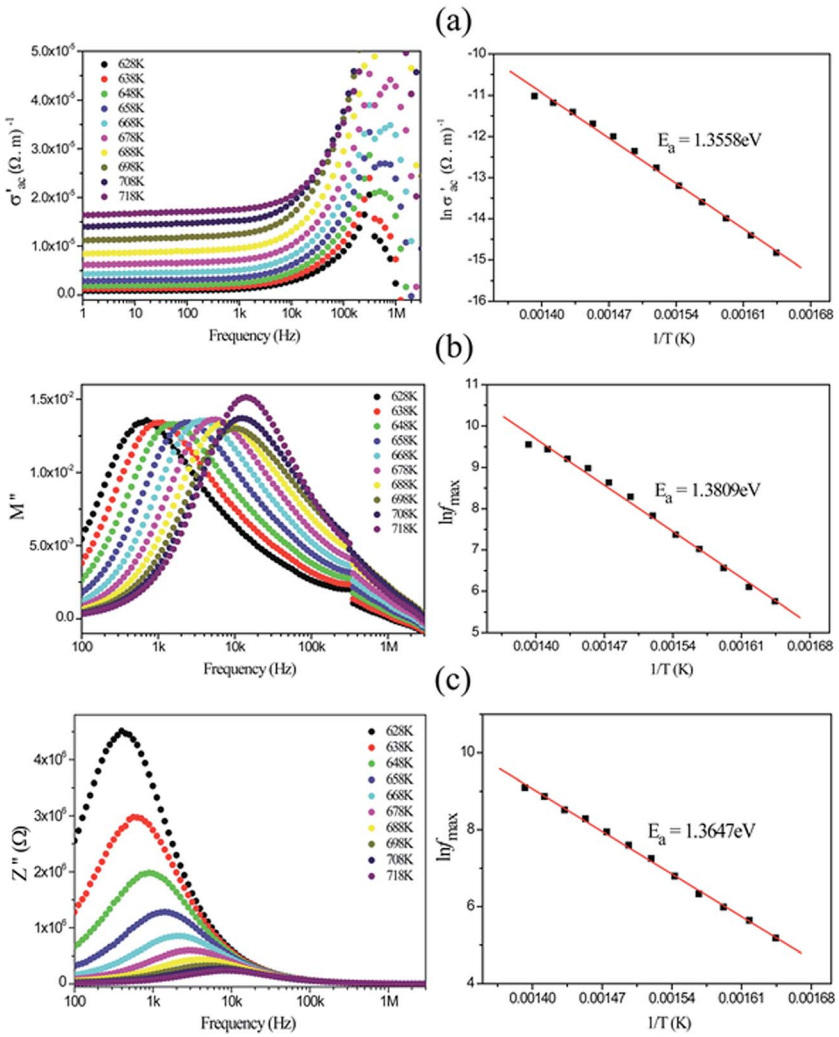

Fig. 5 E_a obtained by temperature shift: (a) conductivity, (b) imaginary electric modulus and (c) imaginary impedance.

In microwaves range (7.84 GHz), the SWO shows high dielectric permittivity ($\varepsilon' = 13.57$) and dielectric loss ($\tan\delta = 0.0281$). This dielectric characterization was performed by Hakki–Coleman method, where was analyzed the TE_{011} mode of the cylindrical resonator. The dielectric properties demonstrated good agreement with results obtained in IS.

The temperature coefficient of resonant frequency (τ_f) for SWO, *i.e.*, the dielectric properties variation with increasing temperature was measured by the SFS method.[30] The τ_f was measured by monitoring of displacement mode HE11δ frequency with increasing of temperature (Fig. 7(a)) and the linear correlation of temperature and HE11δ frequency was observed (Fig. 7(b)). It was possible observed that with the increase of temperature the mode $f_{HE11\delta}$ shifts to smaller frequency. The linear fit with the experimental points were used to calculate τ_f (-207.60 ppm K^{-1}). SWO shows an improbable τ_f values when compared to the results from other materials, where in the literature other double perovskites presented values below 25 ppm K^{-1}.[1,31–35]

For the microwave applications, SWO dielectric resonator was analyzed in the antenna setup (Fig. 1). From this experiment was possible to obtain the main parameter for evaluating the antenna device: return loss (S_{11}), bandwidth and by numerical simulation in HFSS® software. The far field parameters were also obtained as radiation patterns, gain and efficiency of antenna. For the first analysis, the return loss (Fig. 8(a)) presented by SWO-based DRA shows operation frequency ($f_{HE11\delta}$) in 4.12 GHz and return loss (-43.96 dB) below -10 dB, and presents a good coupling and operating as an antenna (error = 0.75%), as shown in Table 4. Fig. 7 also shows a good agreement between experimental and simulated return loss obtained by numerical simulation and collected data. This condition is necessary for acquisition of accurate far field's parameters.

For validation of the numerical simulation, it is necessary a good agreement of return loss and impedances or Smith chart with experimental data. Fig. 8(b) shows experimental and simulated Smith chart. Both presents inductive characteristics and the simulated results presents minor deviations from

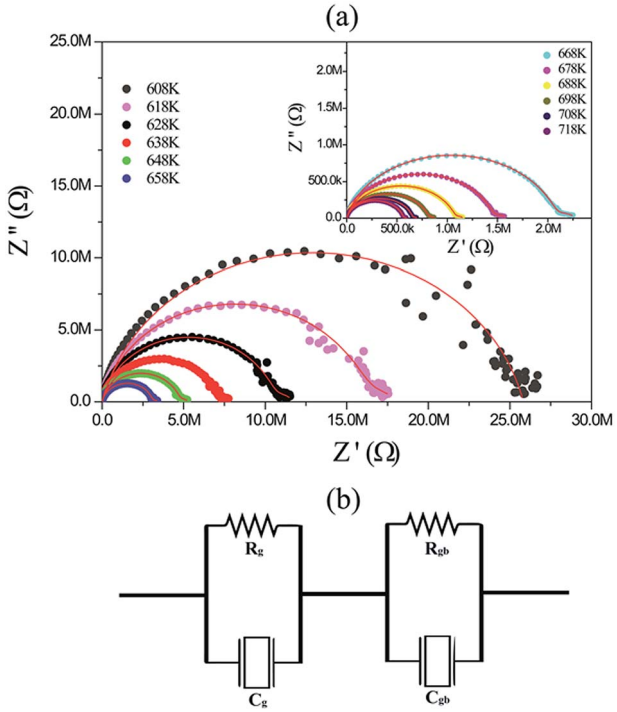

Fig. 6 (a) Nyquist diagram at 608–718 K and fits obtained and (b) equivalent circuit based in the experimental data, where C_g, C_{gb}, R_g and R_{gb} are the resistor–capacitor (RC) circuit associated with the grain (g) and grain boundary (gb) model.

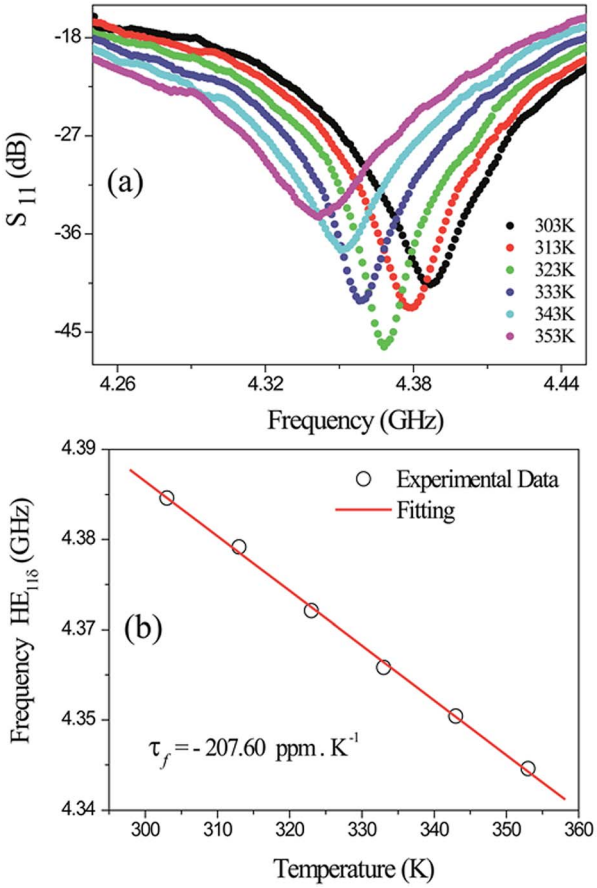

Fig. 7 (a) Displacement of mode $f_{HE11\delta}$ with variation of temperature and (b) temperature coefficient of resonant frequency (τ_f) of SWO.

experimental data. Table 4 summarizes the results obtained by simulations and experimental data, where the DRA presents a bandwidth of 7% or 287 MHz. These results are consistent for DRA characteristics. The gain (1.98 dBi) and efficiency (57.90%) obtained in simulation shows small values compared with another DRAs in the literature.[20,36–39] However, these parameters can be improved by a better coupling between DRA and SMA probe in the antenna device. The radiation profile of DRA is showed in the Fig. 9. One can observed the cylindrical dielectric resonator involved by a simulated radiation patterns. The inset of the Fig. 9 shows that the radiation pattern profile is consistent with a cylindrical DRA, with maximum radiation for $\theta = 0°$ when analyzed by $\varphi = 90°$ and $\varphi = 0°$.

These results shows an antenna device with a good gain and an appreciable efficiency operating at 4.12 GHz. In this sense, to create a device available for Wi-Fi devices (5.15–5.875 GHz)[40] using SWO-based DRA, for example, requires a miniaturization process of this antenna, once the $f_{HE11\delta}$ is a function of

Table 3 Fitting of equivalent circuit parameters for SWO

	Grain			Grain boundary		
T (K)	R_1 (Ω)	P_1	N_1	R_2 (Ω)	P_2	N_2
608	2.71×10^6	9.32×10^{-8}	0.692	2.50×10^7	8.26×10^{-11}	0.883
618	2.26×10^6	7.61×10^{-8}	0.563	1.59×10^7	8.39×10^{-11}	0.888
628	1.30×10^6	9.56×10^{-8}	0.645	1.05×10^7	8.13×10^{-11}	0.896
638	1.17×10^6	2.64×10^{-7}	0.453	6.97×10^6	8.41×10^{-11}	0.897
648	5.57×10^5	1.80×10^{-7}	0.620	4.73×10^6	1.00×10^{-10}	0.884
658	3.49×10^5	3.30×10^{-7}	0.579	3.08×10^6	1.07×10^{-10}	0.882
668	2.07×10^5	5.02×10^{-7}	0.602	2.07×10^6	1.17×10^{-10}	0.877
678	1.42×10^5	6.60×10^{-7}	0.569	1.45×10^6	1.20×10^{-10}	0.878
688	9.96×10^4	1.12×10^{-6}	0.514	1.07×10^6	1.32×10^{-10}	0.875
698	6.83×10^4	1.45×10^{-6}	0.534	8.10×10^5	1.53×10^{-10}	0.867
708	4.83×10^4	2.68×10^{-6}	0.524	6.54×10^5	1.33×10^{-10}	0.877
718	3.85×10^4	3.35×10^{-6}	0.498	5.62×10^5	1.00×10^{-10}	0.895

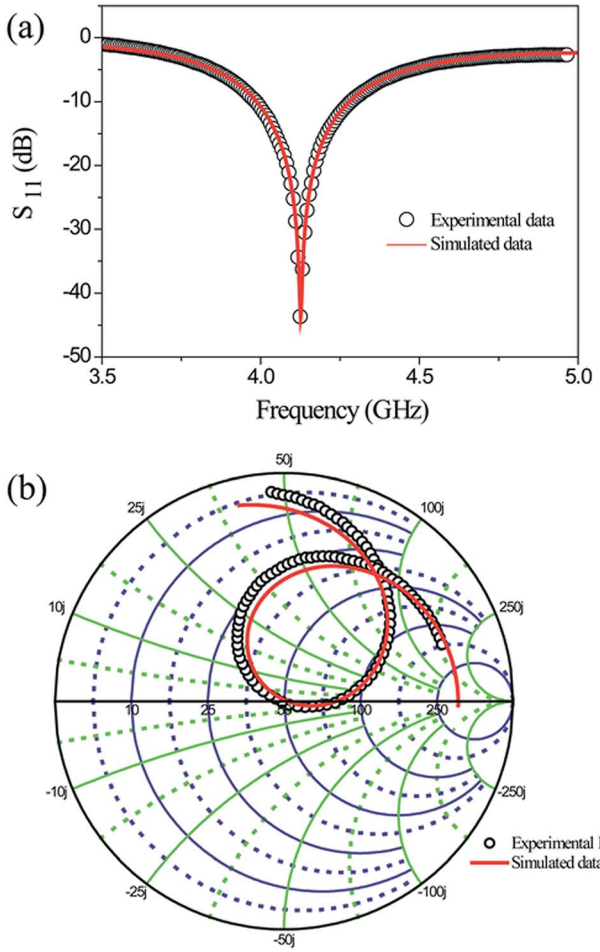

Fig. 8 (a) Experimental and simulated return loss (S_{11}) and (b) Smith chart of the SWO-based DRA.

Table 4 Antenna parameters of the SWO dielectric resonator

	SWO-based DRA		
	Experimental	Simulated	Error (%)
$f_{HE11\delta}$	4.1256	4.1260	0.010
S_{11} (dB)	−43.97	−43.64	0.753
BW (%)	7.268	7.053	2.958
Efficiency (%)		57.90	
Peak resonant resistance (Ω)	108.125	107.155	0.896
Resistance (Ω)	49.702	50.280	1.163
Directivity (dBi)		3.41	
Gain (dBi)		1.98	

dimensions and dielectric properties (see eqn (1)). The better coupling of this novel resonator with the coaxial feed presents gain values closer of commercial antennas (2–3 dBi for residential users). In addition, due to isolating characteristics (higher E_a and impedance ($Z > 1$ GΩ)), higher stable dielectric ($200 < TCC - 5600$ ppm °C^{-1}) and low dielectric permittivity, the

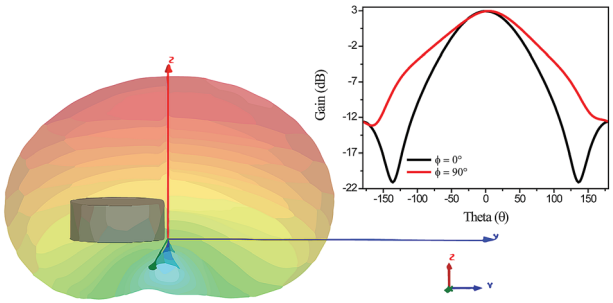

Fig. 9 Radiation profile for DRA. Diagram inset shows radiations in function of θ and φ.

SWO ceramic also can be applied in devices than needs of dielectric class 1.[41,42]

4. Conclusion

The SWO phase was obtained by solid state route and the temperature of synthesis was below that of other works[10,21] due to the previous grinding treatment (activating powder). Dielectric studies showed that SWO presents a transition temperature in 445 K in agreement with previous studies. SWO presented a thermo-activated process with E_a value around 1.35 eV, while showed negative values of TCC. The Nyquist diagrams were well fitted by two associations of R-CPE and the SWO-based DRA presented applicable as microwave antenna. τ_f value for SWO resonator was −207.60 ppm K^{-1} and it is a novel option to be used in association with another phase with positive τ_f values for composite materials to achieve zero τ_f values. The results are important for development of devices that operate in microwaves range, although dielectric properties are frequency-dependent. For example, devices for telecommunications operates in microwaves range as wireless antenna, bluetooth and mobile system. The SWO phase can be also used as dielectric substrates to fabricate microstrip patch antennas. The dielectric ceramic enables miniaturization of this antennas possibility miniaturization of this device and weight reduction.

Acknowledgements

We gratefully acknowledge the financial support of Brazilian Agencies for Scientific and Technological Development CAPES and CNPq.

References

1 S. Vasala and M. Karppinen, *Prog. Solid State Chem.*, 2014, **43**, 1–36.
2 Z.-Y. Wu, C.-B. Ma, X.-G. Tang, R. Li, Q.-X. Liu and B.-T. Chen, *Nanoscale Res. Lett.*, 2013, **8**, 207.
3 L. Jiang, G. Liang, J. Han and Y. Huang, *J. Power Sources*, 2014, **270**, 441–448.
4 Z. Wang, Y. Tian and Y. Li, *J. Power Sources*, 2011, **196**, 6104–6109.

5 P. Zhang, Y.-H. Huang, J.-G. Cheng, Z.-Q. Mao and J. B. Goodenough, *J. Power Sources*, 2011, **196**, 1738–1743.
6 Y. Shimakawa, M. Azuma and N. Ichikawa, *Materials*, 2011, **4**, 153–168.
7 L.-X. Pang and D. Zhou, *J. Mater. Sci.: Mater. Electron.*, 2011, **22**, 807–810.
8 D. Zhou, L.-X. Pang, J. Guo, Z.-M. Qi, T. Shao, Q.-P. Wang, H.-D. Xie, X. Yao and C. A. Randall, *Inorg. Chem.*, 2014, **53**, 1048–1055.
9 D. Zhou, L.-X. Pang, J. Guo, Z.-M. Qi, T. Shao, X. Yao and C. A. Randall, *J. Mater. Chem.*, 2012, **22**, 21412.
10 G. King, A. M. Abakumov, J. Hadermann, A. M. Alekseeva, M. G. Rozova, T. Perkisas, P. M. Woodward, G. Van Tendeloo and E. V Antipov, *Inorg. Chem.*, 2010, **49**, 6058–6065.
11 F. M. Emen and R. Altinkaya, *J. Lumin.*, 2013, **134**, 618–621.
12 X. Zhao, Y. Ding, Z. Li, T. Yu and Z. Zou, *J. Alloys Compd.*, 2013, **553**, 221–224.
13 H. M. Rietveld, *Acta Crystallogr.*, 1967, **22**, 151–152.
14 L. Bleicher, J. M. Sasaki and C. O. Paiva Santos, *J. Appl. Crystallogr.*, 2000, **33**, 1189.
15 R. S. T. M. Sohn, A. A. M. Macêdo, M. M. Costa, S. E. Mazzetto and A. S. B. Sombra, *Phys. Scr.*, 2010, **82**, 055702.
16 M. M. Costa, G. F. M. Pires Júnior and A. S. B. Sombra, *Mater. Chem. Phys.*, 2010, **123**, 35–39.
17 B. W. Hakki and P. D. Coleman, *IEEE Trans. Microwave Theory Tech.*, 1960, **8**, 402–410.
18 W. E. Courtney, *IEEE Trans. Microwave Theory Tech.*, 1970, **18**, 476–485.
19 C. Pascoal, R. Machado and V. C. Pandolfelli, *Ceramica*, 2002, **48**, 61–69.
20 P. M. O. Silva, T. S. M. Fernandes, R. M. G. Oliveira, M. a. S. Silva and A. S. B. Sombra, *Mater. Sci. Eng., B*, 2014, **182**, 37–44.
21 M. Drache, J. Ravez and P. Hagenmuller, *Solid State Commun.*, 1981, **37**, 139–143.
22 L. L. Y. Chang and B. Phillips, *J. Am. Ceram. Soc.*, 1967, **50**, 434–435.
23 C. G. Koops, *Phys. Rev.*, 1951, **83**, 121–124.
24 S. Shafeie, B. Dreyer, R. H. Awater, T. Golod, J. Grins, J. J. Biendicho, S. Y. Istomin and G. Svensson, *J. Solid State Chem.*, 2015, **229**, 243–251.
25 C. Bharti, M. K. Das, A. Sen, S. Chanda and T. P. Sinha, *J. Alloys Compd.*, 2014, **617**, 677–682.
26 C. Bharti, A. Sen, S. Chanda and T. P. Sinha, *J. Alloys Compd.*, 2014, **590**, 125–130.
27 C. Bharti, S. Chanda and T. P. Sinha, *Phys. B*, 2013, **409**, 87–92.
28 C. Bharti, M. K. Das, A. Sen, S. Chanda and T. P. Sinha, *J. Solid State Chem.*, 2014, **210**, 219–223.
29 D. Marrero-López, J. Peña-Martínez, J. C. Ruiz-Morales, M. C. Martín-Sedeño and P. Núñez, *J. Solid State Chem.*, 2009, **182**, 1027–1034.
30 M. A. S. Silva, T. S. M. Fernandes and A. S. B. Sombra, *J. Appl. Phys.*, 2012, **112**, 074106.
31 J. J. Bian, K. Yan and Y. F. Dong, *Mater. Sci. Eng., B*, 2008, **147**, 27–34.
32 J. Y. Wu and J. J. Bian, *Ceram. Int.*, 2012, **38**, 3217–3225.
33 J. Bian, J. Wu, R. Ubic, C. Karthik and Y. Wu, *J. Eur. Ceram. Soc.*, 2015, **35**, 1431–1439.
34 A. Gandhi and S. Keshri, *Ceram. Int.*, 2015, **41**, 3693–3700.
35 J. J. Bian and J. Y. Wu, *Ceram. Int.*, 2016, **42**, 3290–3295.
36 G. N. Rocha, L. F. L. Melo, M. A. S. da Silva, P. V. S. Silva, A. S. B. Sombra and P. B. A. Fechine, *Microw. Opt. Tech. Lett.*, 2012, **54**, 18–23.
37 F. M. M. Pereira, R. S. T. M. Sohn, H. O. Rodrigues, G. F. M. P. Junior, K. R. B. Theophilo, M. J. S. Rocha, M. A. S. Silva and A. S. B. Sombra, *Microw. Opt. Tech. Lett.*, 2010, **52**, 452–458.
38 L. S. Oliveira, D. X. Gouveia, M. A. S. Silva and A. S. B. Sombra, *Microw. Opt. Tech. Lett.*, 2015, **57**, 963–969.
39 A. F. L. Almeida, R. R. Silva, H. H. B. Rocha, P. B. A. Fechine, F. S. A. Cavalcanti, M. A. Valente, F. N. A. Freire, R. S. T. M. Sohn and A. S. B. Sombra, *Phys. B*, 2008, **403**, 586–594.
40 N. t. Ismail, M. T. Ali, N. N. S. N. Dzulkefli, R. Abdullah and S. Omar, in *2012 IEEE Asia-Pacific Conference on Applied Electromagnetics (APACE)*, IEEE, 2012, pp. 283–286.
41 A. Von Hippel, *Dielectric materials and applications*, The Techonology Press of MIT, Cambridge, 1954.
42 A. J. Moulson and J. M. Herbert, *Electroceramics: Materials, Properties, Applications*, Wiley, 2003.